Key Points:
- 3-D shear-velocity structure of the Woodlark Rift, PNG is retrieved
- We observed a localized upper-mantle extension along the Woodlark Rift axis
- Partial melt and/or felsic rocks may exist in the mantle west of DI

Correspondence to:
G. Jin,
ge.jin@ldeo.columbia.edu

Crust and upper mantle structure associated with extension in the Woodlark Rift, Papua New Guinea from Rayleigh-wave tomography

Ge Jin[1], James B. Gaherty[1], Geoffery A. Abers[2], Younghee Kim[3], Zachary Eilon[1], and W. Roger Buck[1]

[1]Lamont-Doherty Earth Observatory of Columbia University, Palisades, New York, USA, [2]Earth and Atmospheric Science, Cornell University, Ithaca, New York, USA, [3]School of Earth and Environmental Sciences, Seoul National University, Seoul, South Korea

Abstract The Woodlark seafloor spreading center is propagating westward into the Australian plate near the D'Entrecasteaux Islands (DI), Papua New Guinea, generating an active transition zone from continental rifting to seafloor spreading. From March 2010 to July 2011, we deployed 31 on-shore and 8 offshore broadband seismic stations around the DI region, to explore the dynamic processes of the lithosphere extension and the exhumation of the high-pressure terranes exposed on those islands. We measure the multiband (10–60 s) Rayleigh-wave phase velocities from both ambient noise and earthquake signals. These measurements are then inverted for a three-dimensional shear-velocity model for the crust and upper mantle. The results indicate that the lithosphere extension is localized near the rift axis beneath the DI, with a shear-velocity structure in the upper mantle that is similar to mid-ocean ridges. Beneath the Kiribisi Basin west of DI, an ultraslow shear-velocity anomaly ($\sim$4.0 km/s) is observed at shallow mantle depth (30–60 km), which can be interpreted either by the presence of excess partial melt due to slow melt extraction, or by the existence of felsic crustal material buried to mantle depth and not yet exhumed.

1. Introduction

The D'Entrecasteaux Islands (DI) of Papua New Guinea locate on the axis of the Woodlark rifting system, which is an active transition zone from continental rifting to seafloor spreading (Figure 1) [e.g., *Taylor et al.*, 1999; *Ferris et al.*, 2006]. These islands expose the high-pressure (HP) metamorphic terranes bearing the youngest-known ultrahigh-pressure (UHP) coesite eclogite [*Monteleone et al.*, 2007; *Zirakparvar et al.*, 2011]. The burial of these HP/UHP rocks is thought to have occurred during the Cenozoic arc-continent collision between the Australian Plate and the Papua New Guinea mainland [e.g., *Lus et al.*, 2004], and they remained at mantle depth until being rapidly exhumed to the surface over the last 5–8 Ma at plate-tectonic rates [e.g., *Baldwin et al.*, 2004, 2008; *Gordon et al.*, 2012]. The exhumation of the UHP rocks is coeval with the local extensional tectonic environment [*Taylor et al.*, 1999].

The exhumation process occurs on the axis of the Woodlark Rift, synchronous with its westward propagation [*Baldwin et al.*, 1993; *Monteleone et al.*, 2007]. The slab pull from the Solomon Sea plate subduction at the New Britain Trench creates a strong extensional environment that favors the exhumation of UHP rocks. There are two competing models to explain the exhumation process in this area: subduction reversal that extracts UHP rocks along the paleosubduction channel as a low-angle unroofing process [*Hill et al.*, 1992; *Webb et al.*, 2008], or thinning of overlying crust that allows penetration of buoyant continental rocks to the surface as diapirs [*Ellis et al.*, 2011; *Little et al.*, 2011].

A numerical modeling study of the diapiric unroofing process requires extremely buoyant crustal bodies and extensive partial melt in the crust and upper mantle [*Ellis et al.*, 2011]. The sporadic volcanism observed across the region may imply the existence of partial melting in upper mantle, with the magmatic composition indicative of subduction enrichment [e.g., *Smith and Davies*, 1976; *Martinez and Taylor*, 1996; *Taylor and Huchon*, 2002]. The presence of the high-density Papuan Ultramafic Belt (PUB) within the Papuan Peninsula (Figure 1) [*Davies and Warren*, 1988], potentially overlying lower-density continental crust, provides a possible source of gravity instability to fuel diapir extrusion [*Martinez et al.*, 2001].
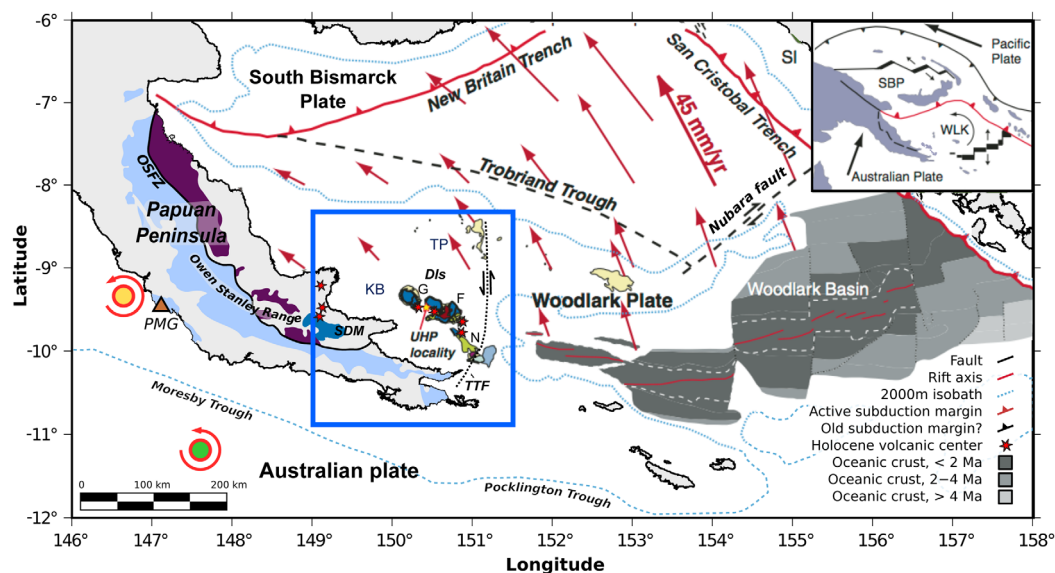
Figure 1. Tectonic map of Papua Peninsula and Woodlark Basin (from *Eilon et al*. [2014], modified after *Baldwin et al*. [2008]). Yellow and green circles are Euler poles for the Woodlark plate (WLK) relative to the Australia plate (AUS) from 6.0 to 0.5 Ma [*Taylor et al*., 1999] and present-day rotation [*Wallace*, 2004], respectively. Red arrows show the current motions of WLK with respect to AUS given by the GPS measurements [*Wallace*, 2004]. Oceanic crust shown by gray shading, Brunes chron indicated by white-dashed line, and the recent shift in tectonics is evident from the obliquity of present spreading ridges to magnetic isochrons. Purple-shaded: PUB (Papuan Ultramafic Belt); light blue shaded: Owen-Stanley Metamorphics. DIs: D'Entrecasteaux Islands (G: Goodenough, F: Fergusson, N: Normanby); KB: Kiribisi Basin; OSFZ: Owen Stanley Fault Zone; SDM: Suckling-Dayman Massif (Dayman Dome); TP: Trobriand Platform; TTF: Trobriand Transfer Fault. Blue box shows area of field deployment in later figures, active volcanic centers in this region only are depicted. Inset: simplified regional tectonics showing role of WLK and South Bismarck Plate (SBP) in mobile belt between obliquely converging Australian and Pacific (PAC) plates.

The youngest high-grade metamorphic rocks locate at Goodenough Island, the western-most of the DI [*Monteleone et al*., 2007]. At the Kiribisi Basin west of Goodenough Island, where potential UHP exhumation may occur in the future, little localized surface extension can be observed in the geology and stratigraphy offshore [*Fitz and Mann*, 2013], while up to 100–140 km extension is required by the far-field plate motion in the last 6 Ma [*Taylor et al*., 1999; *Goodliffe and Taylor*, 2007; *Eilon et al*., 2014]. A recent GPS study reveals that most of the current extension is compensated at the normal faults around the DI and at the Mai'iu fault on the Peninsula [*Wallace et al*., 2014]. Although the mantle deformation estimated from seismic anisotropy suggests a broad mantle flow field [*Eilon et al*., 2014], localized lithospheric extension is observed in the eastern DI [*Abers et al*., 2002; *Eilon et al*., 2015]. The mantle seismic velocity (and inferred lithospheric geometry) and crustal thickness beneath the Kiribisi Basin are important observations to evaluate the lithospheric extension.

From March 2010 to August 2011, 31 land-based broadband stations (Guralp CMG-3T with 120 s-corner sensors) and 8 ocean bottom seismometers (OBS, Trillium 240 with 240 s-corner seismometers) were deployed with a station spacing ~25 km, to cover a 2.5° × 2.5° area centered at Goodenough Island (Figure 2). We perform surface-wave tomography on the collected data and provide a seismic shear-velocity model to reveal the possible distribution of temperature, melt, and compositional anomalies in the crust and the upper mantle, and their possible roles in the UHP unroofing. We find that the mantle extension is localized along the rift axis, and ultraslow shear velocity in the upper mantle beneath the Kiribisi Basin implies the potential existence of partial melt and/or felsic crustal material.

2. Methodology and Data

We image the crust and mantle to approximately 90 km depth in the region using Rayleigh waves derived from a combination of ambient noise and teleseismic earthquakes. Ambient noise and earthquake-based Rayleigh-wave tomography are highly complementary, in that ambient noise is ideally suited to relatively short periods, while teleseismic Rayleigh waves generally constrain longer periods. In detail, the two sources must be processed separately, but the resulting maps of phase velocity are generally compatible at
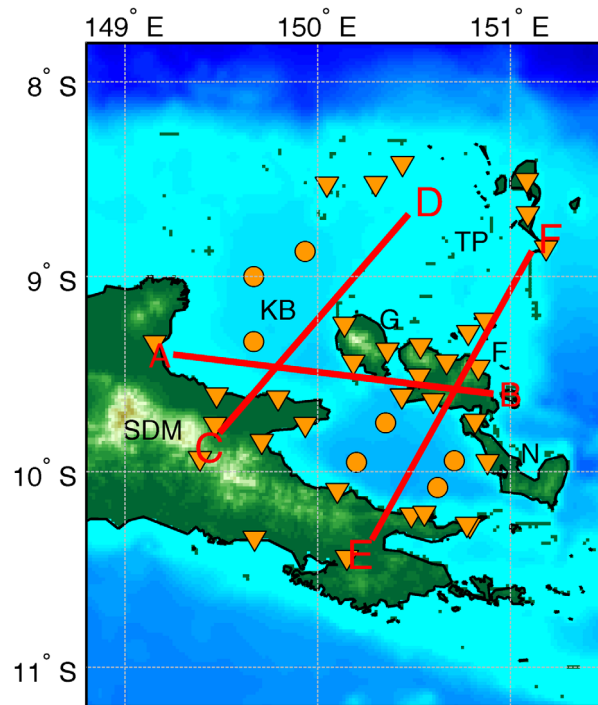
Figure 2. Topography map with station and profile locations. Triangles are land stations while circles are OBSs. Red lines are the profile locations shown in Figure 11. The map labels are the same as in Figure 1.

common periods [e.g., *Yang and Ritzwoller*, 2008; *Foster et al.*, 2014; *Jin and Gaherty*, 2015]. In this study, they can be combined to provide phase-velocity dispersion curves from 10 to 60 s. Here we summarize the analyses utilized to extract phase velocity from each type of data.

2.1. Ambient Noise Tomography

We use ambient noise signals to obtain Rayleigh-wave phase velocities at high frequencies (T < 20 s). To estimate phase velocity, we apply the measurement in the frequency domain to minimize the limitation of short interstation distance at long periods [*Aki*, 1957; *Ekström et al.*, 2009; *Calkins et al.*, 2011]. The stacked cross-spectrum ρ between two vertical records separated by distance r can be represented as:

$$\rho(r, \omega) = \sum_{m=0}^{\infty} i^m a_m(\omega) \mathcal{J}_m \left(\frac{\omega r}{c(\omega)} \right), \quad (1)$$

where $a_m(\omega)$ are the cylindrical harmonic coefficients of the source azimuthal density function, $\mathcal{J}_m$ are the Bessel functions of the first kind, and $c(\omega)$ is the frequency-dependent phase velocity [*Cox*, 1973]. If the source distribution is homogeneous, the only nonzero term of a_m is $a_0 = 1$. The cross-spectrum ρ can be rewritten as [*Aki*, 1957]:

$$\rho(r, \omega) = \mathcal{J}_0 \left(\frac{\omega r}{c(\omega)} \right), \quad (2)$$

In reality, the source distribution may not be azimuthally isotropic, which causes the imaginary part of the cross-spectrum to be nonzero [*Cox*, 1973]. However, this problem can be minimized by properly normalizing the data [*Bensen et al.*, 2007]. We can therefore approximate the real part of the cross-spectrum as:

$$Re(\rho(r, \omega)) = \mathcal{J}_0 \left(\frac{\omega r}{c(\omega)} \right), \quad (3)$$

by ignoring the higher order terms of harmonic expansion [*Ekström et al.*, 2009].

We apply this analysis to the continuous broadband vertical-component records, which are down-sampled to 1 Hz and then divided into hour-long segments. After removing the instrument responses, we normalize the traces by applying the running-absolute-mean technique in the time domain to eliminate the effects of large earthquakes [*Bensen et al.*, 2007]. Then the normalized cross-spectrum is calculated by stacking the hourly coherency spectrum [*Ekström*, 2013]:

$$\rho(\omega) = \frac{1}{N} \sum_{i}^{N} \frac{U_i(\omega) V_i^*(\omega)}{|U_i(\omega)||V_i(\omega)|}, \quad (4)$$

where U_i and V_i are the Fourier transform of the ith time-segment records of two stations.

The cross spectra $\rho(\omega)$ can be transformed back to the time domain to examine the data quality. Figure 3 shows the stacked cross spectra in the time domain after two different band-pass filters. Clean Rayleigh-wave Green's functions can be observed in the period band 10–20 s. The data quality is low at higher frequency band (6–9 s), with asymmetric waveforms and high noise level. This is probably caused by uneven distribution of the secondary microseismic sources [e.g., *Stehly et al.*, 2006; *Tian and Ritzwoller*, 2015].
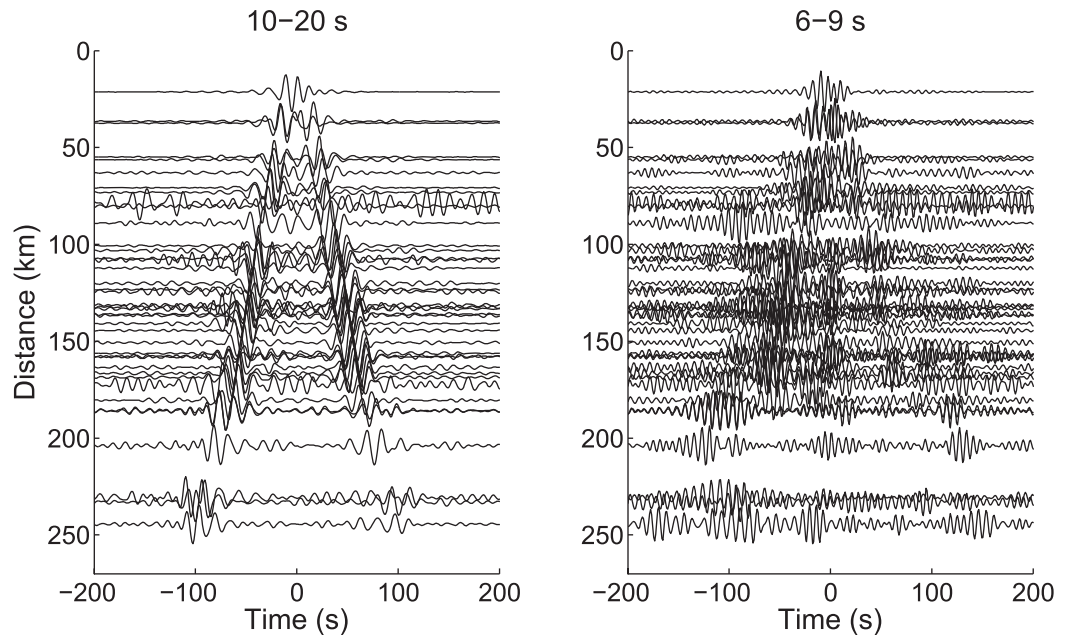
Figure 3. Time-domain ambient noise cross-correlation waveforms of station AGAN to all the other stations. (left) Cross-correlation waveforms filtered between 10 and 20 s. (right) Cross-correlation waveforms filtered between 6 and 9 s.

Ekström et al. [2009] developed a method to estimate dispersion curves in frequency domain by tracking the zero-crossing locations of Bessel functions. With ω_n denoting the frequency of the nth zero-crossing and z_n representing the nth zero of $\mathcal{J}_0$, the phase velocity c at ω_n can be represented as:

$$c(\omega_n) = \frac{\omega_n r}{z_n}. \tag{5}$$

This technique is robust but can still have problems with short-path station pairs, since phase velocities only at zero-crossing frequencies can be measured, and other parts of the dispersion curve have to be interpolated. This issue is particularly important in this study, in which the array's aperture is small. By assuming an average phase velocity of 3.2 km/s, the zero-crossing intervals of $\mathcal{J}_0$ being close to π, and a frequency band ranging from 0.04 to 0.15 Hz (6–20 s), the expected number of zero crossings is:

$$N = \frac{\omega_{max} - \omega_{min}}{c\pi} r \approx 0.07r, \tag{6}$$

where r is in km. For the station pairs with interstation path shorter than 70 km, which comprise 30% of all the possible station pairs in this study, only 4–5 data points can be retrieved to constrain the entire dispersion curve.

In order to better estimate phase velocities from the short-path station pairs, we instead fit the entire cross-spectrum waveforms in the frequency band of interest via a nonlinear least square inversion. Equation (3) can be rewritten as:

$$Re(\rho(r, \omega)) = \mathcal{J}_0\left(\frac{\omega r}{c(\omega)}\right) = \mathcal{J}_0(\omega t(\omega)), \tag{7}$$

where $t(\omega) = r/c(\omega)$ is the phase-delay time (or travel time) between the two stations, and is the unknown variable to be determined. We invert for $t(\omega)$ by minimizing the penalty function ε^2 defined by:

$$\varepsilon^2 = \sum ||\alpha \mathcal{J}_0(\omega t) - Re(\rho)||^2 + a\sum ||\nabla^2 t||^2 + b\sum \left\| \frac{dt}{d\omega} X\left(\frac{dt}{d\omega}\right) \right\|^2. \tag{8}$$
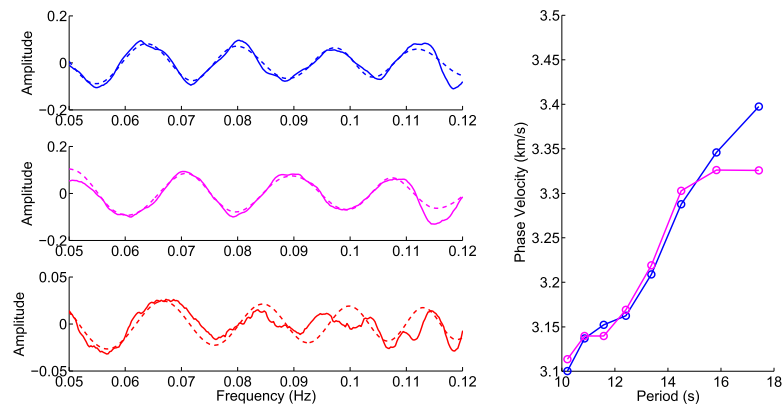
Figure 4. Examples of cross-spectrum waveform fitting. (left) Solid lines are observations and dashed lines are fitting results. Blue lines are from a land-land station pair (AGAN and MAYA), magenta lines are from a land-OBS pair (AGAN and D), while red lines are from an OBS-OBS pair (E and H). Measurements from OBS-OBS pairs are discarded due to the low SNR. (right) Dispersion curves from the Bessel function fittings in the left plot.

X is a step function, with $X(x \geq 0) = 1$ and $X(x < 0) = 0$, and α is a scaling factor to match the amplitude of $\mathcal{J}_0$ with the observation, which is recalculated in each iteration.

The penalty function ε^2 has three components. The first term on the right-hand side is the misfit of the predicted Bessel function to the observation, the second-term quantifies the smoothness of dispersion curve, and the third-term forces the dispersion to be "normal" within the frequency band, i.e., requires the phase velocity to be slower at higher frequency. The constants a and b are the coefficients that control the weighting of the damping terms. During the inversion, the dispersion curve is down-sampled to 5.5 mHz to decrease the number of unknowns. Examples of the Bessel function fitting can be seen in Figure 4. The interstation paths between the station MAYA and the OBS D to the station AGAN are overlapping, and their average dispersion is very similar (Figure 4, right). The discrepancies at long periods are caused by the large Bessel function misfit of the land-OBS pair at low frequencies, probably due to the lower SNR. The OBS-OBS pairs in general have very low SNR for this data set, especially for the frequencies higher than 0.08 Hz (12.5 s). They only provide 7% of the measurements, and are omitted from subsequent inversions.

The phase travel times between 496 station pairs with more than 2000 h of cross-correlation time and high SNR are selected to invert for the 2-D phase-velocity maps at different frequencies. We adopt the ray-theory tomography, and weight each measurement based on the misfit of the Bessel-function fitting and the number of time segments being stacked. Only the station pairs with interstation distances between one and six wavelengths of the Rayleigh waves are included in the tomographic inversion. We apply a smoothness damping by minimizing the second-order gradient of the phase velocities. The phase-velocity maps are generated at 8 periods from 10.2 to 17.4 s. A checkerboard test (see supporting information) shows that anomalies larger than ∼40 km can be well retrieved. Examples of the phase-velocity maps from the ambient noise analysis are shown in the first row of Figure 6.

## 2.2. Earthquake Helmholtz Tomography

We use teleseismic surface waves to estimate Rayleigh-wave phase velocities at low frequencies. In this study, we adopt the automated surface-wave measuring system (ASWMS) developed by *Jin and Gaherty* [2015] to retrieve the 2-D phase-velocity maps.

The ASWMS measures the phase variations between nearby stations by calculating the multichannel cross-correlation functions $C_i(t)$ between vertical-component records, which can be summarized as:

$$C_i(t) = F_i * W_c(S_1 \star W_s S_2),\qquad(9)$$

where S_1 and S_2 are the seismic records from two nearby stations, W_S is the window function applied only on the station 2 waveform to isolate the phase of interest (Rayleigh wave in this study), "*" is the convolution operator, "⋆" is the cross-correlation operator, W_c is the window function applied on the cross-correlation waveform to further isolate the coherent signal generated by fundamental Rayleigh waves, and F_i is the ith narrow band filter with the central frequency ω_i.
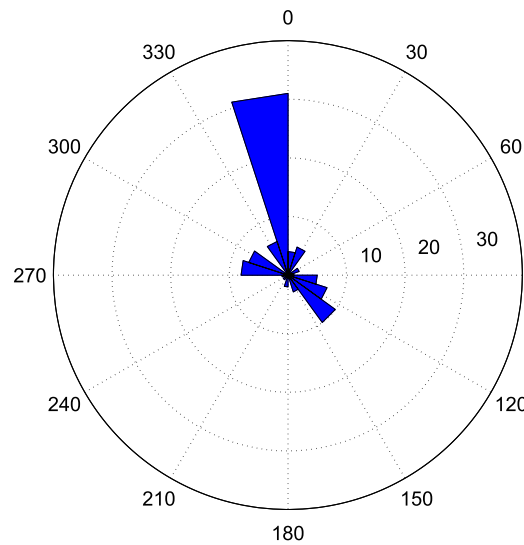
Figure 5. Azimuthal distribution of events for the earthquake-based phase-velocity measurements.

$C_i(t)$ is then fit by a five-parameter wavelet defined as:

$$C_i(t) \approx AGa\big[\sigma(t - t_g)\big]\cos\big[\omega(t - t_p)\big], \quad (10)$$

where the two important variables are the group delay t_g and the phase delay t_p between the two stations, while Ga is the Gaussian function, A is a positive scale factor, σ is the half-bandwidth, and ω is the center frequency of the narrow-band waveform.

The phase delay t_p is then corrected for cycle-skipping and bias generated by the window functions. We define the corrected phase delay as $\delta\tau_p$. In most cases, there is only subtle difference between t_p and $\delta\tau_p$.

We retrieve the corrected phase delays $\delta\tau_p$ from all nearby station pairs within 200 km, and use these measurements to invert for the phase-velocity maps. The Eikonal tomography method [*Lin et al.*, 2009] is modified to adapt to the irregularly spaced arrays [*Jin and Gaherty*, 2015]. The phase delay $\delta\tau_p$ between two stations is written as:

$$\delta\tau_p = \int_{\vec{r}_1}^{\vec{r}_2} \vec{S}(\vec{r})d\vec{r}, \quad (11)$$

where $\vec{r}_1$ and $\vec{r}_2$ are the location vectors of the two stations, and $\vec{S}(\vec{r})$ is the slowness vector field to be solved. The slowness vector field is inverted independently for each event, and the apparent phase velocity can be obtained from the length of the slowness vector: $c' = 1/|\vec{S}(\vec{r})|$.

We then use the amplitude measurements to further correct the phase-velocity maps obtained from the Eikonal tomography. The amplitudes are measured using the auto-correlation functions that are similar to the definition of equation (9), except S_1 is substituted for S_2. The auto-correlation function is then fitted via equation (10), and the scale factor A is a good approximation of the power spectrum amplitude at the center frequency ω_i.

The amplitude measurements are used to correct the Eikonal phase velocity c' for the effect of multipathing via the Helmholtz equation [*Lin and Ritzwoller*, 2011]:

$$\frac{1}{c^2(\vec{r})} = \frac{1}{c'^2(\vec{r})} - \frac{\nabla^2 A(\vec{r})}{A(\vec{r})\omega^2}, \quad (12)$$

where $c(\vec{r})$ is the corrected (structural) phase velocity and $A(\vec{r})$ is the amplitude field. We retrieve individual structural phase-velocity maps for each event, which are then averaged to obtain the final phase-velocity maps at each frequency.

From March 2010 to June 2011, a total of 93 earthquakes with magnitudes larger than 6.0, source depths shallower than 50 km, and epicentral distances from 20° to 140° are selected. The azimuthal distribution of the events is shown in Figure 5. The azimuthal distribution of events is not even, since a large number of eligible earthquakes are from the NNW direction. *Eilon et al.* [2014] report strong azimuthal anisotropy existing in this area. This uneven-distribution of back azimuths may induce some bias in the phase-velocity measurements, which is further discussed in section 3.2.3. The phase velocities obtained using the Helmholtz tomography method is shown in the lower row of Figure 6.

2.3. Shear-Velocity Inversion

We utilize the phase-velocity maps to construct a three-dimensional (3-D) shear-velocity model for the region. At each pixel, dispersion curves are retrieved from the phase-velocity maps, and then inverted for 1-D shear-velocity model. This inversion is known to be strongly dependent on choice of a starting model.
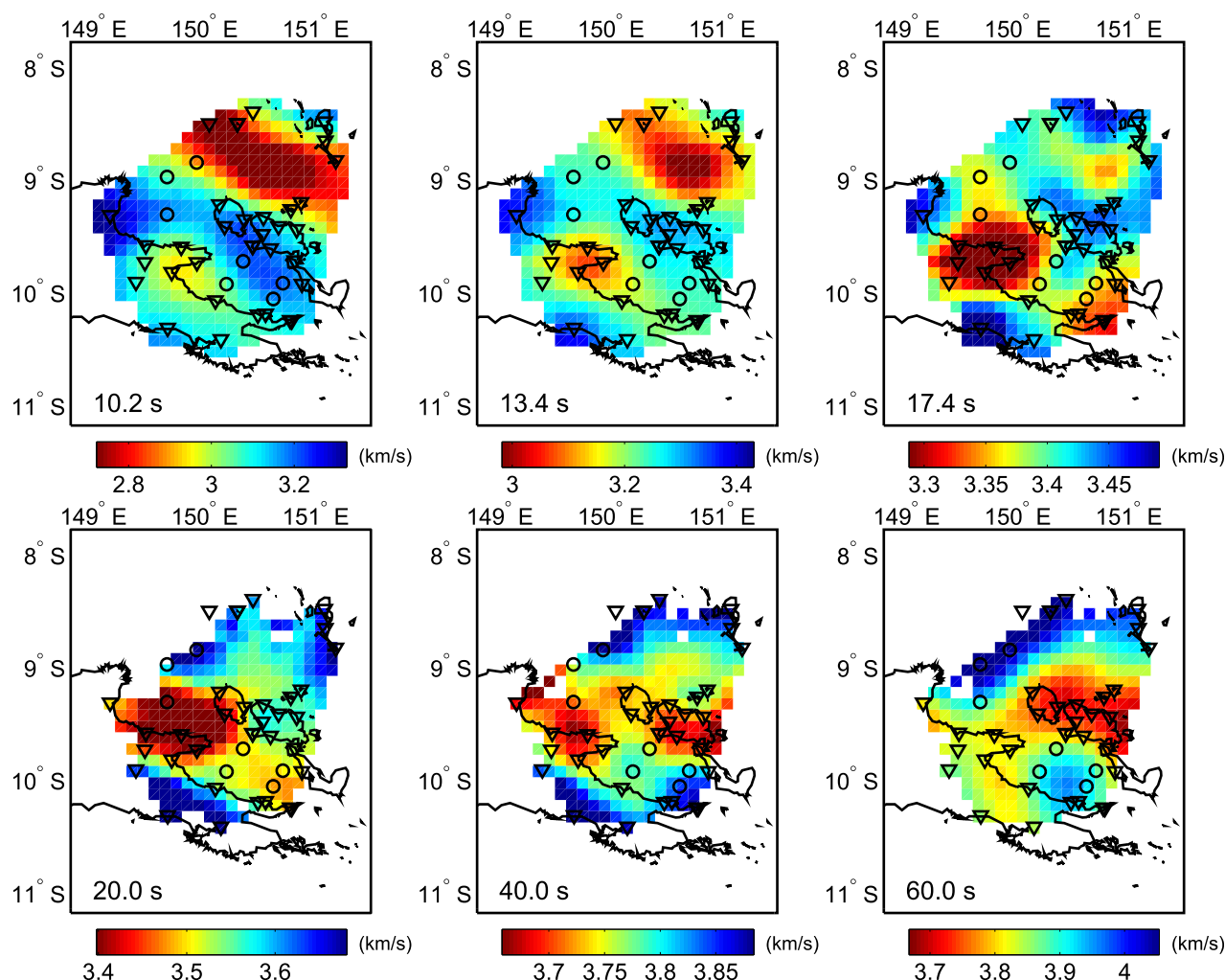
Figure 6. Phase-velocity maps at different periods. The top plots show the results from ambient noise and the bottom plots show the earthquake results. Land stations and OBSs are indicated by triangles and circles, respectively.

In order to minimize and evaluate the effect of the dependence, we develop a strategy that can be divided into three steps: a grid-search for the best initial model, a random perturbation on the best model to generate a large initial model set, and iterative nonlinear least squares inversions to get the final model distribution. The final models from the random initial models are averaged to get the final result.

First, we search through a range of parameters to find a good starting model at each pixel. In this step, the model space is simply divided into three layers: a shallow layer representing sediment or shallow most crustal rocks, a crustal layer with the thickness constrained by the preliminary receiver-function results [*Abers et al.*, 2012; *Obrebski et al.*, 2014], and a half-space layer underneath representing the mantle. The receiver function analysis is based on the H-κ stacking approach [*Zhu and Kanamori*, 2000] to estimate the Moho depth at each station location. These Moho depths are preliminary, but provide a good estimation of first-order crustal thickness variation in the area. We use a minimum-curvature surface fitting to produce a continuous Moho-depth variation across the array. For each pixel, we search through various shallow-layer thicknesses, crustal velocities, and mantle velocities to find the best three-layer model, which provides the minimum misfit to the observed dispersion curve. The parameter space being searched through is listed in Table 1.

Table 1. Initial Model Grid-Search Parameters

| Parameter	Search Values	Unit
Shallow layer thickness	2, 4	km
Shallow layer velocity	2.5 7	km/s
Crustal velocity	3.4, 3.5, 3.6	km/s
Mantle velocity	4.1, 4.3, 4.5, 4.7	km/s
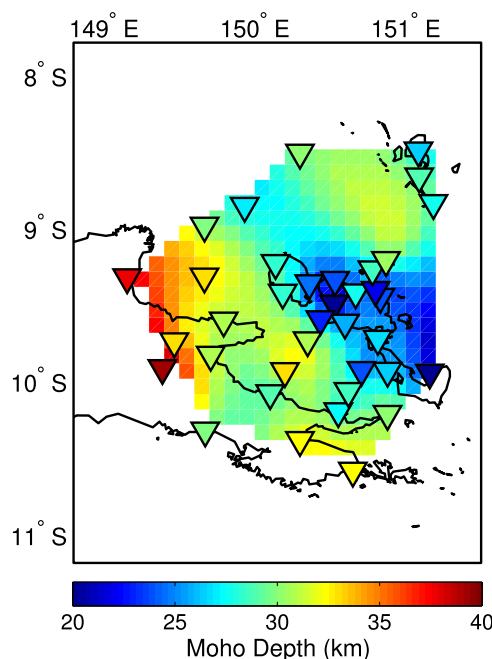
Figure 7. Crustal thickness from the receiver function analysis [*Abers et al.*, 2012]. Values between the stations are interpolated using a minimum-curvature surface.

In order to evaluate the effect of initial model dependency on the resulting model, we randomly perturb the best initial models found in the previous step. At each pixel, all the model parameters are perturbed within a certain range to generate a large set of initial models. The maximum perturbations for the model parameters are: 30% for shallow-layer velocity, 10% for crust and mantle velocities, 5 km for crustal thickness, and 1 km for shallow-layer thickness. For each pixel, we generate 100 random initial models to feed into the later inversion.

We utilize the program *surf96* [*Herrmann and Ammon*, 2004; *Herrmann*, 2013] to invert for detailed 1-D structures of the crust and upper mantle. This program iteratively perturbs the shear velocity of each model layer to fit the observed dispersion curve at a given pixel using an iterative least squares approach. We divide the crust (without the shallow layer) of initial models into four layers with even thickness, and the mantle into 10 layers with a thickness of 10 km. At each iteration, a smoothness damping is applied to the shear-velocity perturbations in the crust and in the mantle separately (no smoothing is applied across the Moho). This procedure ensures the smoothness of final model, while maintaining the velocity discontinuity across Moho if it is required by data.

The nonlinear least squares inversion is performed on the 100 initial models generated in the previous steps at each pixel. Final models with large misfits are discarded (20% larger than the average misfits), with the rest being selected to estimate the mean and standard deviation of the shear velocities at a certain depth.
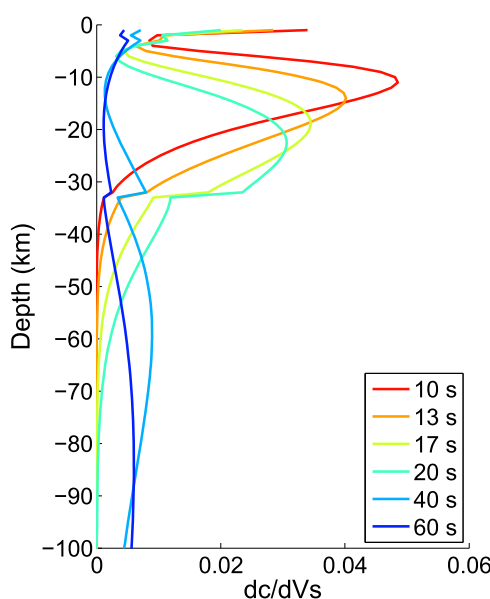
Figure 8. Shear-velocity sensitivity kernels of Rayleigh-wave phase velocities at different frequencies. The kernels are calculated based on a 1-D model with a 32 km crust.

3. Results

3.1. Phase Velocity

Phase-velocity maps of selected periods are shown in Figure 6. In general, phase velocities at higher frequencies are more sensitive to shallower structures. In detail, the sensitivity is highly dependent on the velocity structure. For general earth structure, the peak sensitivity depth is approximately one-third of the surface-wave wavelength.

The highest frequencies (10–15 s) are primarily associated with variation in crustal velocities, including the possible effect of thick sediments in the Trobriand Platform [*Fitz and Mann*, 2013]. The 17 and 20 s phase-velocity maps correlate well with the Moho topography from the preliminary receiver-function results (Figure 7), as the Moho depth variation in the region (20–40 km) [*Abers et al.*, 2002, 2012; *Obrebski et al.*, 2014] corresponds to the peak Rayleigh-wave sensitivity at these periods (Figure 8). For regions with thinner crust (for example, Fergusson and Goodenough Islands), more mantle rocks are sampled and therefore the phase velocity is higher. The consistency between the two

observations shows good reliability of both results. At low frequencies (T > 20 s), the slow anomalies mainly locate along the projection of the Woodlark Rift axis, with the slowest region moving from west to east as period increases.

As presented in section 2, the phase velocities at short periods (10–17 s) and at long periods (20–60 s) are retrieved using different methods. The short-period phase velocities are inverted based on the straight-ray assumption, as the array aperture is not large enough to perform the Eikonal tomography. Theoretically, the straight-ray tomography can be biased by the ray-bending effect. However, *Lin et al.* [2009] show that this bias is fairly small (<0.3%) for short interstation distance, such as used here. The smoothness of the dispersion curves across the transition also implies that this bias is small for our data.

3.2. Shear Velocity

A large part of the shear-velocity uncertainties come from the initial model dependence of the inversion. At each pixel, 100 initial models are randomly generated to invert for shear-velocity profiles. These profiles are then averaged to provide the final result (section 2.3). In general, the standard deviations of the shear velocities from different initial models are smaller than 0.05 km/s at mantle depth (>40 km). The standard deviations are higher around Moho depth (0.1–0.15 km/s), as dispersion curves cannot precisely constrain sharp velocity transitions. The inversion results of several typical locations, together with their uncertainties, are shown in Figure 9. The depth slices and cross sections of the 3-D shear-velocity model are shown in Figures 10 and 11.

These results outline several main features:

1. The axis of the Woodlark rift beneath the DI is identified by slow anomalies with a width about 60 km, extending in depth to the model base.
2. The shallow mantle beneath the Kiribisi Basin west of Goodenough Island (30–60 km, centered around 9.4°S, 149.9°E) is slower than that beneath the eastern DI (Fergusson Island and west of Normanby Island).
3. Mantle velocity beneath the Trobriand Platform and the Papuan Peninsula are notably higher (>4.5 km/s), consistent with stable lithosphere mantle.

Since the period range we use for the inversion is from 10 to 60 s, the structures shallower than 10 km and deeper than 90 km are not well constrained. In addition, the Moho depths of the initial models are constrained by the preliminary receiver-function results. A more formal inversion of receiver function waveforms using dispersion constraint is underway [*Obrebski et al.*, 2014]. Our approach allows us to retrieve a continuous velocity volume, that incorporates the first-order Moho variability, but we do not interpret Moho depth explicitly (Figure 9).

3.2.1. Eastern D'Entrecasteaux Islands

The average shear velocity at 20 km depth is around 3.5 km/s beneath Fergusson Island and west of Normanby Island (Figure 10). This result agrees well with the body-wave tomography result (3.6 km/s) at 23.5 km depth derived from the travel times of local events [*Ferris et al.*, 2006]. Such slow velocities suggest a felsic to intermediate lower-crustal composition, which matches well with the granitic intrusion associated with the metamorphic core complex unroofing observed on the DI [*Ferris et al.*, 2006].

The crust beneath the eastern DI is significantly thinned to ∼20 km, compared to the likely original thickness of 35–40 km seen at off-axis stations [*Abers et al.*, 2002, 2012]. Mantle velocities at this location are low relative to the off-axis regions, implying that the lithosphere has been thinned. This localized crustal and lithospheric extension is likely associated with mantle upwelling, which generates temperature variation and possible partial melt in the upper mantle. The deeper mantle (>60 km) beneath this region has a shear velocity around 4.1 km/s (Figure 9a), which is close to asthenosphere velocities beneath the youngest oceanic lithosphere [*Nishimura and Forsyth*, 1989; *Gu et al.*, 2005], where the mantle geotherm is likely controlled by adiabatic upwelling (Figure 9a).

The upper-most mantle (25–40 km) is slightly faster, with a value ranging from 4.2 to 4.3 km/s. This fast-velocity structure is very similar to the Ethiopian Rift in the east Africa at the similar depth, where the continental lithosphere is thinned due to lateral extension, with the remaining represented by a thin fast seismic lid at the most shallow part of the mantle [*Dugda et al.*, 2007; *Keranen et al.*, 2009].
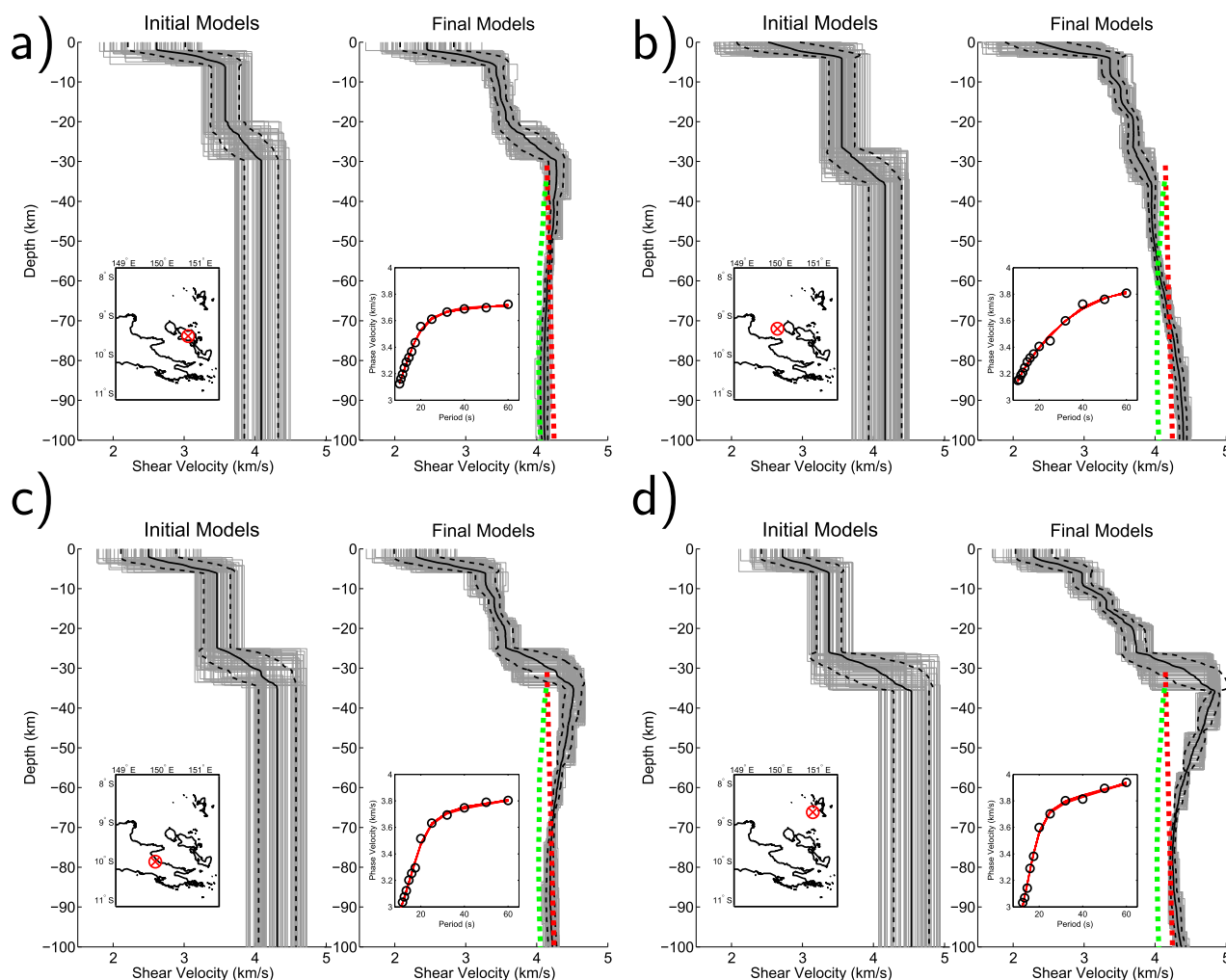
Figure 9. One-dimensional shear-velocity inversions at several example locations. For each subplot, left plot shows the random generated initial models (gray lines), while right plot shows inverted final models. Mean model is represented by solid black line, with dashed black lines indicating 1 standard deviation. The red line from 30 to 100 km in the right plot shows the Vs calculation from mantle adiabatic upwelling model, using the parameters from *Jackson and Faul* [2010], while the green line shows the EPR model from *Gu et al.* [2005]. The embedded map in the left shows the grid location, while the embedded plot in the right shows the inverted phase velocities (red lines) compared to the observations (black circles). (a) Fergusson Island. (b) Kiribisi Basin. (c) Papua Peninsula. (d) Trobriand Platform.

3.2.2. Kiribisi Basin

Figure 9b displays a typical shear-velocity structure beneath the Kiribisi Basin between Goodenough Island and the stratovolcano Mt. Victory. The preliminary receiver-function results suggest a Moho depth around 30–35 km in this region. However, these results are mainly constrained by the OBS measurements, which are not reliable due to the complexity of signals recorded, possibly due to basin reverberations. The shear-velocity model shows no significant velocity discontinuity deeper than 20 km, but displays a gradual velocity increase at shallow depths: from 3.3 km/s in the upper crust (<10 km), to 3.5 km/s at midcrustal depth (10–15 km), to 3.8 km/s in the lower crust depth (>18 km). This crustal structure is similar with the structure along the coastal area of Papua Peninsula northwest of Mt. Victory from previous seismic refraction studies [*Finlayson et al.*, 1976, 1977].

Very slow shear velocities (∼4.0 km/s) are observed at shallow mantle depth from 30 to 60 km beneath this region, which is slower than the mantle beneath the DI at the same depth. Deeper than 60 km, the shear velocity increases with depth, reaching a value of 4.4 km/s at 90 km.

3.2.3. Papua Peninsula and Trobriand Platform

Figures 9c and 9d depict the typical shear-velocity profiles of the Papuan Peninsula and the Trobriand Platform, respectively. These two regions show a similar structure and we interpret them as representing the
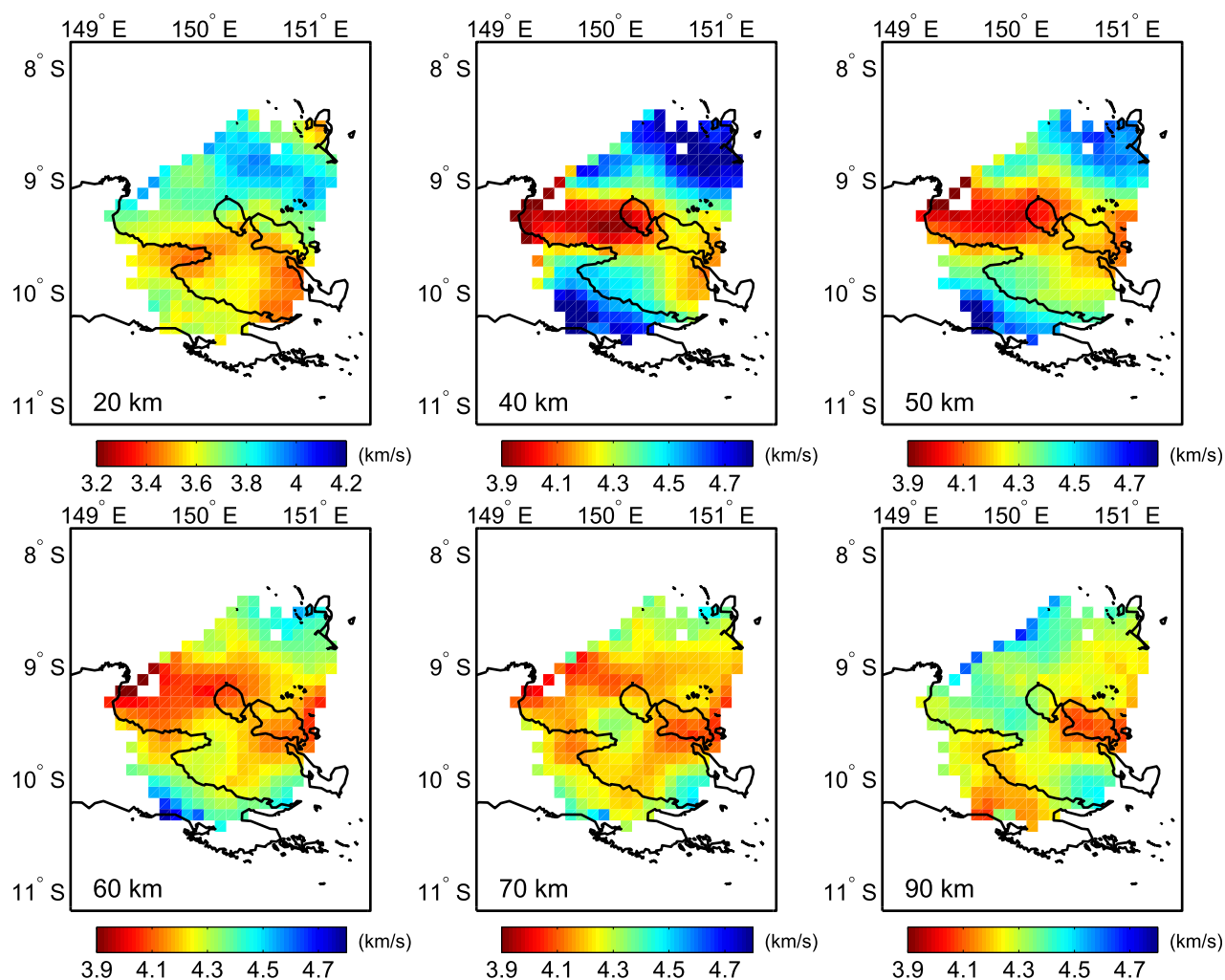
Figure 10. Mean shear velocity at different depths. Depth of 20 km corresponds to mid-to-lower crust, while the plots 40 km and deeper represent variation in the mantle.
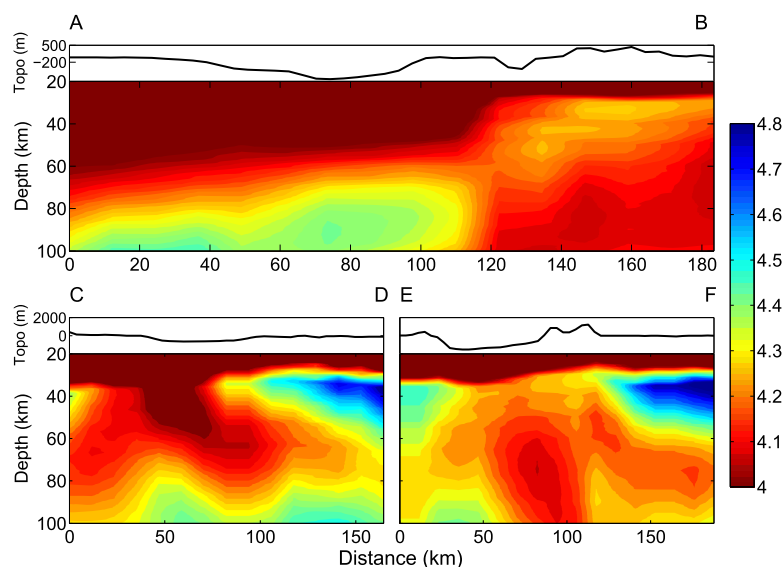
Figure 11. Mean shear velocity along vertical 2-D profiles. The location of profiles can be found in Figure 2.

unrifted continental lithosphere. The receiver function results suggest Moho depth in these regions of ~30–35 km, and the shear-velocity inversion requires a sharp velocity discontinuity at a similar depth.

In the upper mantle, a fast seismic layer exists from the Moho to about 60 km depth. The lithosphere beneath the Trobriand Platform appears much faster than that beneath the Papuan Peninsula. This fast anomaly is at the edge of our array and thus poorly resolved by surface waves, but teleseismic body-wave tomography [*Eilon et al.*, 2015] also shows a significant velocity contrast (~10%) between the Trobriand Platform and the DI at upper-mantle depths (60–120 km). The consistency between these two studies indicates that the fast velocity zone in the upper mantle beneath the Trobriand Platform may be real. *Eilon et al.* [2015] also note the presence of intermediate-depth earthquakes in this region [*Dieck et al.*, 2013], and discuss the interpretation of the anomaly as continental lithosphere or a remnant slab fragment. Alternatively, it is possible that the velocity estimates in this portion of our model are biased high due to anisotropic mantle structure; shear-wave splitting results suggest a strong N-S fabric in this region [*Eilon et al.*, 2014], which corresponds to the strong northward distribution of events used for the earthquake analysis (Figure 5).

4. Discussion

4.1. Localization of Lithospheric Extension

There are significant variations of the extension rate along the Woodlark Rift due to the plate motion geometry. A maximum of ~140 km extension is required west of Goodenough Island and ~200 km east of Normanby Island by the far-field plate motion in the last 6 Ma [*Taylor et al.*, 1999; *Eilon et al.*, 2014]. This ~30% difference in extension may lead to variations in the localization of lithospheric extension along the rift.

In the eastern DI, the seismic observations from this study and previous ones [*Abers et al.*, 2002, 2012; *Eilon et al.*, 2015] are consistent with substantial crustal thinning and lithospheric removal. The exhumed domes, containing rocks that reached maximum pressures of ~3 GPa (100 km) [e.g., *Baldwin et al.*, 2008], currently occupy the space of the original upper crust. Such exhumation may be associated with a strong diapiric mantle upwelling, as modeled by *Ellis et al.* [2011]. However, the shear-velocity profile in this region resembles a mantle structure controlled by adiabatic upwelling. Figure 9a shows the comparisons of our result to the East Pacific Rise [*Gu et al.*, 2005], as well as the calculated shear velocities of dry olivine using the parameterization of *Jackson and Faul* [2010], with the assumptions of 1 cm grain size, 1350°C potential temperature, and adiabatic geotherm extending up to the base of the crust. The slightly slower observed velocity in this study at >60 km depth compared to the predicted shear velocity of dry olivine may be caused by slightly higher potential temperature [*Dalton et al.*, 2014], presence of water and partial melt [*Braun*, 2000], and/or smaller grain size [*Jackson and Faul*, 2010].

The faster upper-most mantle lid (25–40 km) may represent the thinned remnant of the prerift continental lithosphere, perhaps thermally or compositionally modified by the rifting process [e.g., *Schmeling and Wallner*, 2012]. While highly extended continental crust is well documented in mature rifts [e.g., *Keranen et al.*, 2009] and rifted margins [*Shillington et al.*, 2006], observations of thinned mantle lithosphere are relatively few. *Dugda et al.* [2007] find evidence for a thin seismic lid beneath the main Ethiopian rift, with velocities very similar to those observed here. They interpreted the lid as continental lithosphere that was thermally modified by plume impingement associated with rifting, producing velocities that are lower than in the surrounding, unextended lithosphere. There is no evidence for significant thermal perturbation prior to extension in our region, but the velocities in the lid beneath the DEI are lower than in the surrounding peninsula and Trobriand plateau (Figure 9). The prerift lithosphere was likely a complex mélange built up by a recent history of subduction and arc-continent collision [e.g., *Webb et al.*, 2014; *Malusà et al.*, 2015], and this perhaps explains the velocity heterogeneity within the lithosphere. However, it is also plausible that the processes of lower-crustal exhumation and associated volcanism resulted in localized thermal and/or compositional modification of the extended lithosphere, similar to the case in Ethiopia.

Beneath the Kiribisi Basin, west of Goodenough Island, no clear velocity discontinuities can be observed from 10 to 60 km depth (Figure 9b). The Kiribisi Basin is a shallow-water area with presumably thick crust extending north from the Papuan Peninsula, where a seismic refraction study estimates a crustal thickness of ~25 km [*Finlayson et al.*, 1977]. *Fitz and Mann* [2013] use sedimentary records to demonstrate very little (~2–10 km) upper crust extension within the Kiribisi basin since late Miocene, although faults

identified on reflection seismic records sometimes underestimate crustal extension by a significant amount [*Reston*, 2007].

We interpret this region as having a crust about 30 km thick (Figure 7), with relatively fast lower crust and very slow upper mantle, so the velocity contrast between crustal and mantle rocks is small. *Finlayson et al.* [1977] reports the P velocity of the lower crust beneath the west Kiribisi Basin is around 6.5–7.0 km/s, which agrees well with the 3.8 km/s S velocity that we observe, assuming an approximate V_p/V_s ratio of 1.80 [*Ferris et al.*, 2006]. Combined with the very low mantle shear velocities (3.9–4.1 km/s) observed in this region, the seismic expression of the Moho is minimal. The interpretation of the slow mantle velocities is discussed in the next section; in terms of lithospheric breakup, they suggest that such extension is embryonic, and has not yet significantly impacted the crustal structure.

While there is little expression of crustal thinning over thinned mantle lithosphere west of the DI, there is evidence of the extensional processes stepping southward from Goodenough Island onto the Papuan Peninsula. The basin structure southwest of Goodenough Island shows signs of recent extensional faults [*Fitz and Mann*, 2013] and is delineated by a band of active seismicity [*Dieck et al.*, 2013]. The Dayman Dome massif has been interpreted to be an extensional core complex [e.g., *Daczko et al.*, 2011]. The zone of low velocities in the mantle beneath the Kiribisi Basin clearly do not correlate with the trend or locations of these structures. The crustal thickness within the transfer basin southwest of Goodenough Island cannot be well resolved, but stations near Dayman Dome show no evidence of thinned crust in either receiver functions [*Abers et al.*, 2012; *Obrebski et al.*, 2014] or surface-wave velocities.

4.2. Upper Mantle Structure of the Kiribisi Basin

One of the most interesting observations of this study is the extremely slow anomaly (~4.0 km/s) at upper mantle depth beneath the Kiribisi Basin, near 9.4°S, 149.9°E, west of Goodenough Island (e.g., 30–60 km depth, Figure 11). Several mechanisms can affect shear velocity in the upper mantle, including temperature variation, composition, and existence of partial melt. Here we present two possible interpretations of this observation.

The first interpretation is based on the notion that the slow anomaly is generated by temperature variation and partial melt. Assuming that body-wave P-velocity anomalies are controlled entirely by temperature, *Abers et al.* [2002] suggest a 300–700°C temperature difference in the uppermost mantle beneath the eastern DI compared to the surrounding continental lithosphere. *Eilon et al.* [2015] infer a large thermal gradient (up to 700°C difference) at 90 km depth beneath the western DI and the fast seismogenic structure to the northwest, based on body-wave tomography and local seismicity. At 30–60 km depth, the shear velocity in the western Kiribisi Basin is 0.2–0.3 km/s slower than the upper mantle beneath the eastern DI (Figure 11). This is surprising because of the smaller amount of extension in the west. If we try to explain this velocity contrast by purely thermal variation of melt-free dry olivine, it would imply temperatures around 100–200°C higher than the adiabatic temperature at 30–60 km depth, based on the approach of *Jackson and Faul* [2010], and assuming a constant grain size of 1 cm.

For a peridotitic mantle, velocities this low at this depth imply the presence of melt. The presence of water (perhaps emplaced during the long history of subduction in the region) could combine with temperature to lower velocities, but the degree of water necessary would lower the melting temperature such that melting would be induced in this regime as well. It is difficult to determine the abundance of partial melt just by isotropic shear velocity alone, because the melt distribution has great effect on shear velocity and anisotropy [*Bastow et al.*, 2010]. Most studies suggest 2–10% of shear-velocity reduction for each percent of partial melt [e.g., *Takei*, 2002; *Hammond and Humphreys*, 2000; *Takei and Holtzman*, 2009], which is more than enough to explain our observation without much temperature variation.

Why the mantle beneath the less-extended Kiribisi Basin is slower relative to the extended region beneath the DI is unclear. One possible interpretation is that, in the west, the slower and less localized extension near the surface, together with the unthinned continental crust, inhibits melt extraction, and facilitates partial-melt accumulation in the upper mantle. This phenomenon has been proposed in mid-ocean ridge environments where melt production outpaces melt extraction [e.g., *Lizarralde et al.*, 2004; *Gaherty and Dunn*, 2007; *Wei et al.*, 2015]. Teleseismic body-wave tomography [*Eilon et al.*, 2015] observes low velocities

and thus high temperatures at larger depth (>90 km) beneath this region, and thus mantle upwelling may be inducing melting that shallow extension has yet to tap.

In the east, on the other hand, the crustal thinning [*Abers et al.*, 2002], dike intrusion [e.g., *Little et al.*, 2011], and local volcanism [e.g., *Smith*, 1976; *Baldwin et al.*, 2012] on the DI facilitate melt extraction and cooling of the upper mantle. Furthermore, the eastern DI are within 100 km of the Woodlark spreading center tip. Melt extraction associated with building modern oceanic crust may induce an eastward melt propagation, which also helps to generate a E-W gradient of melt abundance in the upper mantle between the eastern DI and the Kiribisi Basin.

The alternative interpretation of the slow anomaly is based on a possible compositional difference. The gneiss domes that form the DI contain a significant amount of felsic material, some of which was subducted to the depth of ~100 km prior to exhumation [e.g., *Baldwin et al.*, 2008; *Little et al.*, 2011]. The U-Pb zircon geochronologic analysis from the Fergusson Island samples yields an exhumation history that suggests the UHP metamorphic eclogites stalled beneath the crust for ~1 Ma, before they were finally exhumed to the surface [*Gordon et al.*, 2012]. Meanwhile, the exhumation propagates to the west, as shown by a westward younging of the ^{40}Ar/^{39}Ar cooling ages of the HP samples within the DI [*Baldwin et al.*, 1993]. These observations suggest the possible presence of felsic, crustal materials in the mantle west of Goodenough Island. This material would have been emplaced through the same (likely subduction-related) process that produced the DI UHP facies, but it has not yet been exhumed.

We evaluate whether a mix of crustal and mantle rocks can explain the slower upper mantle (30–60 km) shear velocity beneath the Kiribisi Basin compared to the eastern DI, where the UHP rocks have been exhumed. *Brownlee et al.* [2011] investigate the samples collected from the DI, and estimate their seismic velocities at depth. Based on their calculation, the quartzofeldspathic gneiss, which is the dominant composition of the gneiss domes, has a shear velocity of ~3.7 km/s at the depth of 30–60 km, assuming a temperature of 700°C. The shear velocity of melt-free olivine at the same P-T condition is 4.6 km/s if 1 cm grain size is assumed [*Jackson and Faul*, 2010]. The average shear velocity we observed in the upper-most mantle beneath the Kiribisi Basin is around 4.0 km/s. In order to achieve this value, about 62% of the mantle volume should be occupied by quartzofeldspathic gneiss (using a Voigt-Reuss-Hill average).

This tectonic setup is similar to the numerical diapir model of *Ellis et al.* [2011]. However, the model requires a 22 km radius subducted crustal body that is mostly made of gneiss, and consists of roughly 10–20% partial melt during exhumation. These conditions would lead to a shear-velocity value much slower than our observation. While the limited resolution of surface-wave tomography [*Bodin and Maupin*, 2008] allows for small partial-melt crustal bodies at upper mantle depth, the size must be much smaller than that modeled by *Ellis et al.* [2011]. Further modeling studies are needed to determine the conditions under which a mixed felsic-mafic body at depth would provide sufficient buoyancy to drive exhumation, while still meeting the constraints of seismic observations.

5. Conclusion

We retrieve a 3-D shear-velocity model in the area near the D'Entrecasteaux Islands, Papua New Guinea using both ambient noise and earthquake Rayleigh-wave phase-velocity measurements.

The results suggest a localized upper-mantle extension along the Woodlark Rift axis, which favors the exhumation of the UHP rocks exposed on the DI. In the eastern DI, the deeper velocity structure (>50 km) is close to the prediction of an adiabatic upwelling mantle, with a slightly faster shallow mantle that may be associated with the extended continental lithosphere. There is no evidence of an ultraslow diapir-like structure [*Ellis et al.*, 2011] presently beneath the DI.

We discover the shallow mantle beneath the Kiribisi Basin west of the DI is slower than the mantle beneath the more extended eastern DI at the same depth. We provide two possible interpretations of this observation: more partial melt accumulates in the west because of the less melt extraction; and/or there are unexhumed felsic crustal material at mantle depth, mixed with peridotitic mantle west of the DI. In either scenario, the degree of partial melt is modest. This low-velocity anomaly is spatially decoupled from the surface expression of extension west of the DI, which occurs tens of kilometer south on the Papuan Peninsula.

References

Abers, G. A., A. Ferris, M. Craig, H. Davies, A. L. Lerner-Lam, J. C. Mutter, and B. Taylor (2002), Mantle compensation of active metamorphic core complexes at Woodlark rift in Papua New Guinea, *Nature*, *418*(6900), 862–865.

Abers, G. A., Y. Kim, J. B. Gaherty, Z. Eilon, G. Jin, and R. Verave (2012), Imaging to understand exhumation of UHP rocks during rifting: The 2010–2011 CDPapua seismic experiment, Abstract T42C-06 presented at 2012 Fall Meeting, AGU, San Francisco, Calif., 3–7 Dec.

Aki, K. (1957), Space and time spectra of stationary stochastic waves, with special reference to microtremors, *Bull. Earthquake Res. Inst. Univ. Tokyo*, *35*, 415–456.

Baldwin, S. L., G. S. Lister, E. J. Hill, D. A. Foster, and I. McDougall (1993), Thermochronologic constraints on the tectonic evolution of active metamorphic core complexes, D'entrecasteaux Islands, Papua New Guinea, *Tectonics*, *12*(3), 611–628, doi:10.1029/93TC00235.

Baldwin, S. L., B. D. Monteleone, L. E. Webb, P. G. Fitzgerald, M. Grove, and E. J. Hill (2004), Pliocene eclogite exhumation at plate tectonic rates in eastern Papua New Guinea, *Nature*, *431*(7006), 263–267.

Baldwin, S. L., L. E. Webb, and B. D. Monteleone (2008), Late Miocene coesite-eclogite exhumed in the Woodlark Rift, *Geology*, *36*(9), 735–738, doi:10.1130/G25144A.1.

Baldwin, S. L., P. G. Fitzgerald, and L. E. Webb (2012), Tectonics of the New Guinea Region, *Annu. Rev. Earth Planet. Sci.*, *40*(1), 495–520, doi:10.1146/annurev-earth-040809-152540.

Bastow, I. D., S. Pilidou, J. M. Kendall, and G. W. Stuart (2010), Melt-induced seismic anisotropy and magma assisted rifting in Ethiopia: Evidence from surface waves, *Geochem. Geophys. Geosyst.*, *11*, Q0AB05, doi:10.1029/2010GC003036.

Bensen, G. D., M. H. Ritzwoller, M. P. Barmin, A. L. Levshin, F. Lin, M. P. Moschetti, N. M. Shapiro, and Y. Yang (2007), Processing seismic ambient noise data to obtain reliable broad-band surface wave dispersion measurements, *Geophys. J. Int.*, *169*(3), 1239–1260, doi:10.1111/j.1365-246X.2007.03374.x.

Bodin, T., and V. Maupin (2008), Resolution potential of surface wave phase velocity measurements at small arrays, *Geophys. J. Int.*, *172*(2), 698–706, doi:10.1111/j.1365-246X.2007.03668.x.

Braun, M. (2000), The effects of deep damp melting on mantle flow and melt generation beneath mid-ocean ridges, *Earth Planet. Sci. Lett.*, *176*(3–4), 339–356, doi:10.1016/S0012-821X(00)00015-7.

Brownlee, S. J., B. R. Hacker, M. Salisbury, G. Seward, T. A. Little, S. L. Baldwin, and G. A. Abers (2011), Predicted velocity and density structure of the exhuming Papua New Guinea ultrahigh-pressure terrane, *J. Geophys. Res.*, *116*, B08206, doi:10.1029/2011JB008195.

Calkins, J. A., G. A. Abers, G. Ekström, K. C. Creager, and S. Rondenay (2011), Shallow structure of the Cascadia subduction zone beneath western Washington from spectral ambient noise correlation, *J. Geophys. Res.*, *116*, B07302, doi:10.1029/2010JB007657.

Cox, H. (1973), Spatial correlation in arbitrary noise fields with application to ambient sea noise, *J. Acoust. Soc. Am.*, *54*(5), 1289–1301, doi:10.1121/1.1914426.

Daczko, N. R., P. Caffi, and P. Mann (2011), Structural evolution of the Dayman dome metamorphic core complex, eastern Papua New Guinea, *Geol. Soc. Am. Bull.*, *123*(11–12), 2335–2351, doi:10.1130/B30326.1.

Dalton, C. A., C. H. Langmuir, and A. Gale (2014), Geophysical and geochemical evidence for deep temperature variations beneath mid-ocean ridges, *Science*, *344*(6179), 80–83, doi:10.1126/science.1249466.

Davies, H. L., and R. G. Warren (1988), Origin of eclogite-bearing, domed, layered metamorphic complexes ("core complexes") in the D'entrecasteaux Islands, Papua New Guinea, *Tectonics*, *7*(1), 1–12, doi:10.1029/TC007i001p00001.

Dieck, C. C., G. A. Abers, Z. Eilon, J. B. Gaherty, and R. Verave (2013), Seismicity in an active rift exposing ultra-high pressure metamorphic rocks: D'Entrecasteaux Islands, Papua New Guinea, Abstract T21A-2524 presented at 2013 Fall Meeting, AGU, San Francisco, Calif.

Dugda, M. T., A. A. Nyblade, and J. Julia (2007), Thin lithosphere beneath the Ethiopian plateau revealed by a joint inversion of Rayleigh wave group velocities and receiver functions, *J. Geophys. Res.*, *112*, B08305, doi:10.1029/2006JB004918.

Eilon, Z., G. A. Abers, and G. Jin (2014), Anisotropy beneath a highly extended continental rift, *Geochem. Geophys. Geosyst.*, *15*, 545–564, doi:10.1002/2013GC005092.

Eilon, Z., G. A. Abers, J. B. Gaherty, and G. Jin (2015), Imaging continental breakup using teleseismic body waves: The Woodlark Rift, Papua New Guinea, *Geochem. Geophys. Geosyst.*, *16*, 2529–2548, doi:10.1002/2015GC005835.

Ekström, G. (2013), Love and Rayleigh phase-velocity maps, 5–40 s, of the western and central USA from USArray data, *Earth Planet. Sci. Lett.*, *402*, 42–49, doi:10.1016/j.epsl.2013.11.022.

Ekström, G., G. A. Abers, and S. C. Webb (2009), Determination of surface-wave phase velocities across USArray from noise and Aki's spectral formulation, *Geophys. Res. Lett.*, *36*, L18301, doi:10.1029/2009GL039131.

Ellis, S. M., T. A. Little, L. M. Wallace, B. R. Hacker, and S. J. H. Buiter (2011), Feedback between rifting and diapirism can exhume ultrahigh-pressure rocks, *Earth Planet. Sci. Lett.*, *311*(3–4), 427–438, doi:10.1016/j.epsl.2011.09.031.

Ferris, A., G. A. Abers, B. Zelt, B. Taylor, and S. Roecker (2006), Crustal structure across the transition from rifting to spreading: The Woodlark rift system of Papua New Guinea, *Geophys. J. Int.*, *166*(2), 622–634.

Finlayson, D. M., K. J. Muirhead, J. P. Webb, G. Gibson, A. S. Furumoto, R. J. S. Cooke, and A. J. Russell (1976), Seismic Investigation of the Papuan Ultramafic Belt, *Geophys. J. Int.*, *44*(1), 45–59, doi:10.1111/j.1365-246X.1976.tb00274.x.

Finlayson, D. M., B. J. Drummond, C. Collins, and J. B. Connelly (1977), Crustal structures in the region of the Papuan Ultramafic Belt, *Phys. Earth Planet. Inter.*, *14*(1), 13–29.

Fitz, G., and P. Mann (2013), Tectonic uplift mechanism of the goodenough and Fergusson Island gneiss domes, eastern Papua New Guinea: Constraints from seismic reflection and well data, *Geochem. Geophys. Geosyst.*, *14*, 3969–3995, doi:10.1002/ggge.20208.

Foster, A., G. Ekström, and M. Nettles (2014), Surface wave phase velocities of the Western United States from a two-station method, *Geophys. J. Int.*, *196*(2), 1189–1206, doi:10.1093/gji/ggt454.

Gaherty, J. B., and R. A. Dunn (2007), Evaluating hot spot-ridge interaction in the Atlantic from regional-scale seismic observations, *Geochem. Geophys. Geosyst.*, *8*, Q05006, doi:10.1029/2006GC001533.

Goodliffe, A. M., and B. Taylor (2007), The boundary between continental rifting and sea-floor spreading in the Woodlark Basin, Papua New Guinea, *Geol. Soc. Spec. Publ.*, *282*(1), 217–238, doi:10.1144/SP282.11.

Gordon, S. M., T. A. Little, B. R. Hacker, S. A. Bowring, M. Korchinski, S. L. Baldwin, and A. R. C. Kylander-Clark (2012), Multi-stage exhumation of young UHP–HP rocks: Timescales of melt crystallization in the D'Entrecasteaux Islands, southeastern Papua New Guinea, *Earth Planet. Sci. Lett.*, *351–352*, 237–246, doi:10.1016/j.epsl.2012.07.014.

Gu, Y. J., S. C. Webb, A. L. Lam, and J. B. Gaherty (2005), Upper mantle structure beneath the eastern Pacific Ocean ridges, *J. Geophys. Res.*, *110*, B06305, doi:10.1029/2004JB003381.

Hammond, W. C., and E. D. Humphreys (2000), Upper mantle seismic wave velocity: Effects of realistic partial melt geometries, *J. Geophys. Res.*, *105*(B5), 10,975–10,986, doi:10.1029/2000JB900041.

Herrmann, R. B. (2013), Computer programs in seismology: An evolving tool for instruction and research, *Seismol. Res. Lett.*, *84*(6), 1081–1088, doi:10.1785/0220110096.

Herrmann, R. B., and C. J. Ammon (2004), *Computer Programs in Seismology: Surface Waves, Receiver Functions, and Crustal Structure*, version 3.30, St. Louis Univ., Saint Louis, Mo.

Hill, E. J., S. L. Baldwin, and G. S. Lister (1992), Unroofing of active metamorphic core complexes in the D'Entrecasteaux Islands, Papua New Guinea, *Geology*, *20*(10), 907–910, doi:10.1130/0091-7613(1992)020<0907:UOAMCC>2.3.CO;2.

Jackson, I., and U. H. Faul (2010), Grainsize-sensitive viscoelastic relaxation in olivine: Towards a robust laboratory-based model for seismological application, *Phys. Earth Planet. Inter.*, *183*(1–2), 151–163, doi:10.1016/j.pepi.2010.09.005.

Jin, G., and J. B. Gaherty (2015), Surface wave phase-velocity tomography based on multichannel cross-correlation, *Geophys. J. Int.*, *201*(3), 1383–1398, doi:10.1093/gji/ggv079.

Keranen, K. M., S. L. Klemperer, J. Julia, J. F. Lawrence, and A. A. Nyblade (2009), Low lower crustal velocity across Ethiopia: Is the Main Ethiopian Rift a narrow rift in a hot craton?, *Geochem. Geophys. Geosyst.*, *10*, Q0AB01, doi:10.1029/2008GC002293.

Lin, F.-C., and M. H. Ritzwoller (2011), Helmholtz surface wave tomography for isotropic and azimuthally anisotropic structure, *Geophys. J. Int.*, *186*(3), 1104–1120, doi:10.1111/j.1365-246X.2011.05070.x.

Lin, F.-C., M. H. Ritzwoller, and R. Snieder (2009), Eikonal tomography: Surface wave tomography by phase front tracking across a regional broad-band seismic array, *Geophys. J. Int.*, *177*(3), 1091–1110, doi:10.1111/j.1365-246X.2009.04105.x.

Little, T. A., B. R. Hacker, S. M. Gordon, S. L. Baldwin, P. G. Fitzgerald, S. Ellis, and M. Korchinski (2011), Diapiric exhumation of Earth's youngest (UHP) eclogites in the gneiss domes of the D'Entrecasteaux Islands, Papua New Guinea, *Tectonophysics*, *510*(1–2), 39–68, doi:10.1016/j.tecto.2011.06.006.

Lizarralde, D., J. B. Gaherty, J. A. Collins, G. Hirth, and S. D. Kim (2004), Spreading-rate dependence of melt extraction at mid-ocean ridges from mantle seismic refraction data, *Nature*, *432*(7018), 744–747, doi:10.1038/nature03140.

Lus, W. Y., I. McDougall, and H. L. Davies (2004), Age of the metamorphic sole of the Papuan Ultramafic Belt ophiolite, Papua New Guinea, *Tectonophysics*, *392*(1–4), 85–101, doi:10.1016/j.tecto.2004.04.009.

Malusà, M. G., C. Faccenna, S. L. Baldwin, P. G. Fitzgerald, F. Rossetti, M. Laura Balestrieri, M. Danišík, A. Ellero, G. Ottria, and C. Piromallo (2015), Contrasting styles of (U)HP rock exhumation along the Cenozoic Adria-Europe plate boundary (Western Alps, Calabria, Corsica), *Geochem. Geophys. Geosyst.*, *16*, 1786–1824, doi:10.1002/2015GC005767.

Martinez, F., and B. Taylor (1996), Backarc spreading, rifting, and microplate rotation, between transform faults in the Manus Basin, *Mar. Geophys. Res.*, *18*(2–4), 203–224, doi:10.1007/BF00286078.

Martinez, F., A. M. Goodliffe, and B. Taylor (2001), Metamorphic core complex formation by density inversion and lower-crust extrusion, *Nature*, *411*(6840), 930–934, doi:10.1038/35082042.

Monteleone, B. D., S. L. Baldwin, and L. E. Webb (2007), Late Miocene–Pliocene eclogite facies metamorphism, D'Entrecasteaux Islands, SE Papua New Guinea, *J. Metamorph. Geol.*, *25*(2), 245–265 doi:10.1111/j.1525-1314.2006.00685.x.

Nishimura, C. E., and D. W. Forsyth (1989), The anisotropic structure of the upper mantle in the Pacific, *Geophys. J. Int.*, *96*(2), 203–229, doi:10.1111/j.1365-246X.1989.tb04446.x.

Obrebski, M., G. A. Abers, G. Jin, and Z. Eilon (2014), Rift structure in Eastern Papua New Guinea from the joint inversion of receiver functions and seismic noise, Abstract T54A-07 presented at 2014 Fall Meeting, AGU, San Francisco, Calif., 14–18 Dec.

Reston, T. (2007), Extension discrepancy at North Atlantic nonvolcanic rifted margins: Depth-dependent stretching or unrecognized faulting?, *Geology*, *35*(4), 367–370, doi:10.1130/G23213A.1.

Schmeling, H., and H. Wallner (2012), Magmatic lithospheric heating and weakening during continental rifting: A simple scaling law, a 2-D thermomechanical rifting model and the East African Rift System, *Geochem. Geophys. Geosyst.*, *13*, Q08001, doi:10.1029/2012GC004178.

Shillington, D. J., W. S. Holbrook, H. J. A. Van Avendonk, B. E. Tucholke, J. R. Hopper, K. E. Louden, H. C. Larsen, and G. T. Nunes (2006), Evidence for asymmetric nonvolcanic rifting and slow incipient oceanic accretion from seismic reflection data on the Newfoundland margin, *J. Geophys. Res.*, *111*, B09402, doi:10.1029/2005JB003981.

Smith, I. E. (1976), *Volcanism in Australasia*, pp. 275–286, Elsevier, N. Y.

Smith, I. E., and H. L. Davies (1976), *Geology of the Southeast Papuan Mainland*, Aust. Gov. Publ. Serv. for the Bur. of Miner. Resour., Geol. and Geophys., Canberra, Australia.

Stehly, L., M. Campillo, and N. M. Shapiro (2006), A study of the seismic noise from its long-range correlation properties, *J. Geophys. Res.*, *111*, B10306, doi:10.1029/2005JB004237.

Takei, Y. (2002), Effect of pore geometry on VP/VS: From equilibrium geometry to crack, *J. Geophys. Res.*, *107*(B2), 2043, doi:10.1029/2001JB000522.

Takei, Y., and B. K. Holtzman (2009), Viscous constitutive relations of solid-liquid composites in terms of grain boundary contiguity. 1: Grain boundary diffusion control model, *J. Geophys. Res.*, *114*, B06205, doi:10.1029/2008JB005850.

Taylor, B., and P. Huchon (2002), Active continental extension in the western Woodlark Basin: A synthesis of Leg 180 results, *Proceedings of the Ocean Drilling Program, Scientific Results*, in edited by P. Huchon, B. Taylor, and A. Klaus, pp. 1–36, U.S. Gov. Print. Off., Washington, D. C.

Taylor, B., A. M. Goodliffe, and F. Martinez (1999), How continents break up: Insights from Papua New Guinea, *J. Geophys. Res.*, *104*(B4), 7497–7512, doi:10.1029/1998JB900115.

Tian, Y., and M. H. Ritzwoller (2015), Directionality of ambient noise on the Juan de Fuca plate: Implications for source locations of the primary and secondary microseisms, *Geophys. J. Int.*, *201*(1), 429–443, doi:10.1093/gji/ggv024.

Wallace, L. M. (2004), GPS and seismological constraints on active tectonics and arc-continent collision in Papua New Guinea: Implications for mechanics of microplate rotations in a plate boundary zone, *J. Geophys. Res.*, *109*, B05404, doi:10.1029/2003JB002481.

Wallace, L. M., S. Ellis, T. Little, P. Tregoning, N. Palmer, R. Rosa, R. Stanaway, J. Oa, E. Nidkombu, and J. Kwazi (2014), Continental breakup and UHP rock exhumation in action: GPS results from the Woodlark Rift, Papua New Guinea, *Geochem. Geophys. Geosyst.*, *15*, 4267–4290, doi:10.1002/2014GC005458.

Webb, L. E., S. L. Baldwin, T. A. Little, and P. G. Fitzgerald (2008), Can microplate rotation drive subduction inversion?, *Geology*, *36*(10), 823–826, doi:10.1130/G25134A.1.

Webb, L. E., S. L. Baldwin, and P. G. Fitzgerald (2014), The Early-Middle Miocene subduction complex of the Louisiade Archipelago, southern margin of the Woodlark Rift, *Geochem. Geophys. Geosyst.*, *15*, 4024–4046, doi:10.1002/2014GC005500.

Wei, S. S., D. A. Wiens, Y. Zha, T. Plank, S. C. Webb, D. K. Blackman, R. A. Dunn, and J. A. Conder (2015), Seismic evidence of effects of water on melt transport in the Lau back-arc mantle, *Nature*, *518*(7539), 395–398, doi:10.1038/nature14113.

Yang, Y., and M. H. Ritzwoller (2008), Teleseismic surface wave tomography in the western U.S. using the Transportable Array component of USArray, *Geophys. Res. Lett.*, *35*, L04308, doi:10.1029/2007GL032278.

Zhu, L., and H. Kanamori (2000), Moho depth variation in southern California from teleseismic receiver functions, *J. Geophys. Res.*, *105*(B2), 2969–2980, doi:10.1029/1999JB900322.

Zirakparvar, N. A., S. L. Baldwin, and J. D. Vervoort (2011), Lu–Hf garnet geochronology applied to plate boundary zones: Insights from the (U)HP terrane exhumed within the Woodlark Rift, *Earth Planet. Sci. Lett.*, *309*(1–2), 56–66, doi:10.1016/j.epsl.2011.06.016.